On the nucleation of deformation twins at the early stages of plasticity

Hamidreza Abdolvand[1*], Karim Louca[1], Charles Mareau[2], Marta Majkut[3,4], Jonathan Wright[3]

[1]Department of Mechanical and Materials Engineering, Western University, London, Ontario, N6A 5B9, Canada

[2]Arts et Metiers ParisTech, Campus d'Angers, LAMPA, 2 Boulevard du Ronceray, 49035, Angers Cedex 1, France

[3]ESRF, 71 Avenue Des Martyrs, 38000 Grenoble, France

[4] AMVALOR Metz , Technopole METZ 2000, 4 rue Augustin Fresnel, 57070 Metz, France

On the nucleation of deformation twins at the early stages of plasticity

Hamidreza Abdolvand[1*], Karim Louca[1], Charles Mareau[2], Marta Majkut[3,4], Jonathan Wright[3]

[1]Department of Mechanical and Materials Engineering, Western University, Spencer Engineering Building, London, Ontario, N6A 5B9, Canada

[2]Arts et Metiers ParisTech, Campus d'Angers, LAMPA, 2 Boulevard du Ronceray, 49035, Angers Cedex 1, France

[3]ESRF, 71 Avenue Des Martyrs, 38000 Grenoble, France

[4] AMVALOR Metz , Technopole METZ 2000, 4 rue Augustin Fresnel, 57070 Metz, France

Abstract

Understanding the deformation mechanisms of hexagonal close-packed (HCP) polycrystals at the grain scale is crucial for developing both macro and micro scale predictive models. Slip and twinning are the two main deformation mechanisms of HCP polycrystals at room temperature. In this paper, the development of grain-level stress tensors during nucleation and growth of twins is investigated. A pure zirconium specimen with HCP crystals is deformed *in-situ* while the centre-of-mass, orientation, elastic strain, and stress of individual grains are measured by three-dimensional synchrotron X-ray diffraction (3D-XRD). The observed microstructure is subsequently imported into a crystal plasticity finite element (CPFE) model to simulate the deformation of the polycrystal. The evolution of stress in twin-parent pairs at the early stages of plasticity, further into plasticity zone, and unload is studied. It is shown that twins do not relax very much at the nucleation step, but the difference between the measured stress in the twin and parent increases further into plastic zone where twins relax. While at the early stages of plasticity all six twin variants are active, a slightly better estimation of active variants is obtained using the measured grain-resolved stress tensors.

Keywords: Hexagonal close-packed crystals, Zirconium, Synchrotron X-ray Diffraction, crystal plasticity finite element, twinning

1. Introduction

Understanding the deformation mechanisms of polycrystalline materials has been at the centre of many studies for decades. In metals and alloys, plastic deformation is controlled by the movement of dislocations on a particular plane in a particular direction, i.e. slip. In the absence of "easy" slip systems, deformation twinning may become active where a discrete domain of the crystal reorients to accommodate the applied strain through the twin transformation strain. In hexagonal close-packed (HCP) polycrystals deformation by twinning is often active. When all twinned zones orient towards one unique direction, a large macroscopic strain equal to the twin transformation strain will be observed; however, when different variants of the same twin system become active, the effects of the transformation strain from different twins will be homogenised. While it is known that the formation of a twin alters the local state of stress within the parent grain, it has proven to be challenging to quantify the state of deformation within the parent and the twin. This paper focuses on quantifying the evolution of stress in twin and parent pairs, and on how different twin variants become active while deforming a polycrystalline zirconium specimen.

Since deformation twins nucleate and grow with mechanical loading, it is challenging to measure elastic strains within twins, especially at the early stages of plasticity when the size of twins is small. Diffraction based experimental techniques are mainly used to quantify load partitioning between twins and parents [1–9]. For example, the development of internal lattice strains during twinning and detwinning of magnesium alloys is studied using neutron diffraction [10–12]. It is generally shown that changing the direction of applied load directly affects twinning and detwinning. The lattice strains measured with neutron diffraction have significantly improved our understanding of load sharing between twin and parent grains, yet in such measurements, the local interactions between grains is usually homogenized. Such interactions can be characterized using higher resolution techniques. For example, three dimensional synchrotron micro-Laue X-ray diffraction was used to study twinning and de-twinning in Mg alloys where it was shown that lattice strains measured inside a parent decrease towards the twin interface [13]. Using the same technique, Kumar et al [14] measured the stress tensor within a parent grain and showed that the stress is localized at the vicinity of the twin boundary. While these studies provide valuable insight into understanding twinning, they are mainly conducted on a few twin-parent pairs.

A better statistical analysis of twins can be provided by the use of electron diffraction [15–18]. For this purpose, the high angular resolution electron back scatter diffraction (HR-EBSD) technique is mainly used [19–21]. For example, Guo et al [22] used HR-EBSD to measure localized stress fields around twins in titanium. They showed that, a better estimation of active twin variant can be achieved if the measured local stresses are used for determining Schmid factor. With the use of the same technique, Khosravani et al [23] showed that, while both first and second predominant twin variants are active in magnesium, slip transfer from a soft grain to a hard grain can trigger formation of twins in the hard grain. In this context, grains that have "easy" slip systems and undergo plastic deformation by prism or basal are called plastically "soft" whereas those that lack easy slip systems are called plastically "hard" grains. In addition, nano-beam electron diffraction was recently used to understand how strain fields around twin boundaries are affected by twin morphologies. It was observed that elastic strains accumulate at the vicinity of semi-coherent twin boundaries within the parent grain [24].

In addition to experimental measurements, numerical modelling techniques have been used to understand the interactions between twins and parent grains [25], twins and twins [26], and twins and slip bands [27]. For modelling twins at meso-scales, crystal plasticity is used in the self-consistent [28–31], fast Fourier transform (FFT) [32], and finite element frameworks [33,34]. For example, Want et al [31] have recently developed a self-consistent model for simulating twinning and de-twinning in magnesium. They found that less internal strain develops in hard grains surrounded by hard neighbouring grains. By adapting the self-consistent framework, Barrett et al [35] studied the

deformation behaviour of α-uranium and found that twinning and de-twinning control the response of uranium during a load reversal. In addition, Grilli et al [36] used crystal plasticity finite element (CPFE) to characterise slip and twin activity in the same material. It was shown that for replicating the experimental data measured by digital image correlation, it was important to consider the interactions between coplanar twins in full-field models. More recently, the CP-FFT full-field modelling scheme was used for studying twins [37,38]. For example Paramatmuni and Kanjarla [39] have developed a CP-FFT model to study the interaction of twins and their corresponding parents. This model shows that the evolution of stress in parents and twins depends on their misorientation with respect to the loading direction.

The further development of full-field numerical models requires the measurement of comprehensive experimental data sets that can explain the interaction between twins and their corresponding parents. In this paper, three-dimensional synchrotron X-ray diffraction is used to measure the evolution of stress in individual twin and parent pairs. The centre-of-mass (COM), orientation, relative volume, elastic strain, and stress for individual grains is measured during in-situ deformation of a pure zirconium specimen. Post-processing procedures are developed to find twins and their corresponding parents and track them during early stages of plasticity, further into the plasticity zone, as well as unload. Special focus is given to evolution of stress within the identified pairs and variant selection at the early stages of macroscopic plasticity.

2. Experiment

2.1 The experiment

Specimens were cut from a pure zirconium bar that was heat-treated at 650 °C for two days and subsequently slow cooled to room temperature. The heat treatment was done to recrystallize grains and reduce as much as possible the residual stresses that existed in the bar. The tensile specimen was cut from the radial-transverse face of the bar with the c-axis of HCP crystals oriented towards and perpendicular to the loading direction. The pole figure of the specimen, measured with EBSD prior to the 3D-XRD experiment, is shown in Fig. 1a. The specimen was cut using electrical discharge machining with the geometry shown in Fig 1b. The final cross section of the specimen after mechanical and electro- polishing was 0.78mm x 0.67mm.

The in-situ 3D-XRD experiment was conducted at ID11 at the European Synchrotron Radiation Facility (ESRF), France. The coordinate system of the specimen is shown in Fig. 1b and is defined based on the loading direction (LD), X-ray beam direction (BD), and transverse direction (TD). The experiment was carried out by illuminating the specimen with a planar beam of monochromatic X-rays with the energy set at 78.395 keV. The beam height was initially set at 40 µm where 25 layers of the specimen were measured to cover 1 mm height of the specimen. To avoid overlapping of broadened diffraction peaks, the height of the beam was reduced to 25 µm towards the end of the experiment and the number of scanned layers increased to 40 to cover the same specimen volume. The specimen was mounted on an ADMET tensile rig and was deformed with the average strain rate of 10^{-5} s^{-1}. The axial force was measured by a load cell and the applied strain was monitored by a strain gauge attached to the specimen. For collecting diffraction patterns, the specimen was rotated around the LD in the angular range of [−234.5º to −125.5º] and [−54.5º to 54.5º] at the step size of 0.25º. The diffraction patterns were collected on a Frelon2K detector with 2048 x 2048 pixels with each pixel size of 50 x 50 µm². The distance between the specimen and the detector was fixed at approximately 312 mm.
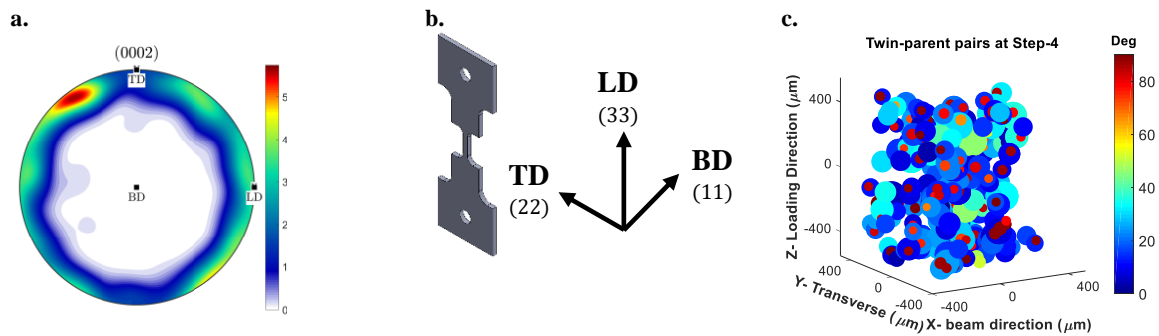
Fig. 1. (a) The measured (0002) pole figure of the undeformed specimen. (b) A schematic of the specimen with the coordinate system used in this paper. (c) An example of the twin-parent pairs found in Step-4. Grains are colour coded with respect to their c-axis misorientation with the loading direction and the size of each sphere is proportional to the measured relative volume of the grain. In (a) and (b) LD, BD, and TD refer to loading, X-ray beam, and transverse directions.

Diffraction patterns were collected at 9 different loading steps; in the first step, Step-1, the specimen was preloaded to 8 MPa (see Fig 2c). The collected patterns at this step were used to calibrate the single crystal lattice parameters of pure zirconium. In the Step-2, the specimen was deformed to an axial strain of 0.257% , which is in the elastic zone but close to the onset of plasticity. This was followed by three more measurements performed at the early stages of macroscopic plasticity, i.e., at the applied strains of 0.355%, 0.565%, and 1.087% for Step-3, Step-4, and Step-5, respectively. In addition, three more measurement steps were performed in the plastic zone where the specimen was deformed up to 2.6%. The specimen was finally unloaded in Step-9 and the residual stresses were measured. For each measurement step, firstly the positions of the grips of the deformation rig were fixed, the specimen was realigned, and diffraction patterns were subsequently collected. During the alignment and pattern collection, the specimen relaxed, and creep was observed in the gauge length of the specimen. Both macroscopic stress and strain were recorded for CPFE modelling.

2.2 Post-processing procedure

The post-processing of the collected patterns was mainly done by developing python codes to use the subroutines embedded in Fable (https://github.com/FABLE-3DXRD) and ImageD11 for peaksearching and indexing grains. Once grains of each layer were identified, they were used to reconstruct the 3D grain maps by adding layers and merging the common grains. Peaks assigned to each grain were used to determine 12 grain properties: three positions, three orientations, and six strain components or lattice parameters (a ,b, c, α, β, γ) [40]. On average, more than 97 peaks were assigned to each grain allowing to determine both grain properties and "errors" associated with them. The method used for calculating errors is explained in Oddershede et al [41]. At the preload, a set of initial lattice parameters were defined to calculate elastic strains for individual grains. The weighted average of the corresponding stress was then calculated and used for adjusting the "stress-free" lattice parameters. This procedure was conducted for the seven layers of the probed volume. An average of the acquired lattice parameters from the seven layers was subsequently used for calculating strains across the all 25 layers. When the stress from all layers was equal to the applied stress, the initial lattice parameters were deemed to be converged. The fitted lattice parameters for preload were used, without any alteration, for all other loading steps to determine elastic strain within individual grain. Also, at the preload and unload steps, any deviation from the "stress-free" lattice parameters was assumed to arise from residual stresses.

Since the scope of this study is to investigate the evolution of stress within individual grains, the measured 3D maps from each step were compared to other steps to match grains following the procedure described in [42,43]. The grains that were not matched between any two consecutive steps were considered as potential twins that nucleated in between the steps. For determining twin-parent

pairs, the layer at which the twin was found was firstly determined and codes were developed to search for a parent grain in the same layer in the vicinity of the twin. A twin-parent pair is defined when (a) one of the variants of $\{10\bar{1}2\}$ tensile twinning system could be identified as the common habit plane, (b) the misorientation between the c-axis of the twin and the parent was $85.25°\pm1.5°$, (c) the distance between the twin and parent was less than the summation of their radii and (d) only one unique parent could be identified. With the procedures developed for matching twin-parent pairs in this paper, it was possible to determine grains with multiple twins.

3. Crystal plasticity model

The development of accurate constitutive models for simulating nucleation and propagation of twins in the finite element framework is an active research area [44–48]. In this paper, however, CPFE modelling is used to investigate the evolution of stress *only* in the parent grains and to simulate how the crystallographic texture evolves with formation of twins. A detailed numerical study discussing constitutive modelling of twins is underway. The details of the model used for simulating plastic deformation by slip and twinning can be found in [49], only a brief description and the changes made to the model is provided here. The total velocity gradient (L) can be decomposed to its elastic (L^e) and plastic (L^p) parts, where in the presence of twinning, L^p at each integration point (IP) can be written as:

$$L^p = (1 - f^{tw}) \sum_{\alpha=1}^{N^s} S^\alpha \dot{\gamma}^\alpha + \sum_{t=1}^{N^{tw}} S^t \dot{\gamma}^t \qquad (1)$$

where S represents the Schmid tensor that can be calculated using the dyadic product of the normal to the slip/twinning plane and slip/twinning direction. N^s and N^{tw} represent the number of slip and twinning systems and f^{tw} is the relative volume of the twin at a given IP. Here, we assume that no plasticity takes place in the twinned zone and that the stress in the twin is equal to that in the parent.

The shear strain rate ($\dot{\gamma}^\alpha$) on each slip or twinning system is calculated using a rate-dependent equation [50]:

$$\dot{\gamma}^\alpha = \dot{\gamma}_0^\alpha \left|\frac{\tau^\alpha}{g^\alpha}\right|^n sign(\frac{\tau^\alpha}{g^\alpha}) \qquad (2)$$

where $\dot{\gamma}_0^\alpha$ is the reference shear rate of the slip or twin system, τ^α is the resolved shear stress acting on the slip or twinning plane and g^α is the current critical resolved shear stress (CRSS) for the slip or twining system. It can be assumed that the evolution of twin volume fraction ($\dot{f}^{tw}$) correlates with $\dot{\gamma}^t$, i.e. $\dot{f}^{tw} = \frac{\dot{\gamma}^t}{\gamma_0^{tw}}$, where γ_0^{tw} is the characteristic twin shear, which is 0.169 for zirconium. The resolved shear stress (τ^α) on each slip system is calculated using the symmetric part of the Schmid tensor (P^α) and the Kirchhoff stress (Ψ):

$$\tau^\alpha = P^\alpha : \Psi \qquad (3)$$

The Jaumann rate of Kirchhoff stress ($\breve{\Psi}$) is calculated as:

$$\breve{\Psi} = \mathbb{C} : D^e \text{ where } \breve{\Psi} = \dot{\Psi} - \Omega^e \Psi + \Psi \Omega^e \qquad (4)$$

where $\mathbb{C}$ is the stiffness tensor, and D^e and Ω^e are the elastic parts of the deformation rate and spin tensor, respectively. They can be calculated using the symmetric and asymmetric parts of L^e.

The strength of each slip system (g^α) is assumed to follow an extended Voce hardening rule [51]:

$$g^\alpha = g_0^\alpha + (g_1^\alpha + \theta_1^\alpha \Gamma)\left(1 - exp\left(-\frac{\theta_0^\alpha \Gamma}{g_1^\alpha}\right)\right) \qquad (5)$$

where g^α is the current CRSS, g_0^α is the initial CRSS, Γ is accumulated shear on all slip/twinning systems, θ_0^α is initial hardening rate, and g_1^α and θ_1^α determine asymptotic characteristics of hardening. A cubic volume with the side length of 400 μm, located in the centre of the 3D-XRD probed volume was meshed for CPFE modelling. First order cubic elements (C3D8) were used for meshing the simulation cube. To assign a grain orientation to each element, the weighted Voronoi tessellation scheme described in Abdolvand et al [52] was used:

$$C_i = \left\{ X \in R^d \,\middle|\, \|X - s_i\|^2 - w_i^2 < \|X - s_j\|^2 - w_j^2, i \neq j \right\} \tag{6}$$

where X is the position vector of the element C_i in the cube, s_i is the position vector of the seed point of the grain i, and w_i is the radius of the same grain measured by 3D-XRD. To determine the seed point of each grain, Eq. 6 is solved in two steps. In the first step, s_i is replaced by the measured COM_i of the grain G_i. This results in a new COM_b for G_i which does not necessarily coincide with the actual measured COM_i. In the second iteration, s_i is set equal to $2COM_b - COM_i$. An example of the simulation cube imported into Abaqus FE solver is shown in Fig. 2a where 10^6 IPs were used to discretise 1335 grains, i.e., more than 749 IPs per grain.

To simulate the experiment, the model was first cooled down to room temperature to model the thermal residual stresses that develop during the heat treatment. The coefficients of thermal expansion for single crystal zirconium are 5.3 x10^{-6} and 10.1x10^{-6} 1/°C along the crystal a- and c-axis, respectively [53]. Although the positions of the grips were fixed during each measurement step and total elongation of the specimen was constant, deformation creep was observed over the gauge of the specimen. Hence, the "as-measured" strain rate of each step was applied to the model as a velocity. This was done by dividing each measurement step into three sub-steps; in the first sub-step, the specimen was deformed to a peak load, in the second sub-step the specimen relaxed while realigning, and in the third sub-step the specimen relaxed during the collection of diffraction patterns. The recorded strain and time at the beginning and end of each sub-step were used to calculate the applied velocity to the model. In Fig 2b, the recorded strain-time during the experiment is compared with the calculated one from the CPFE model. It can be seen that the applied velocity successfully replicates the measured strain-time curve. In Fig. 2c, the corresponding stress-strain curve from the CPFE model is compared to the one measured during the experiment.
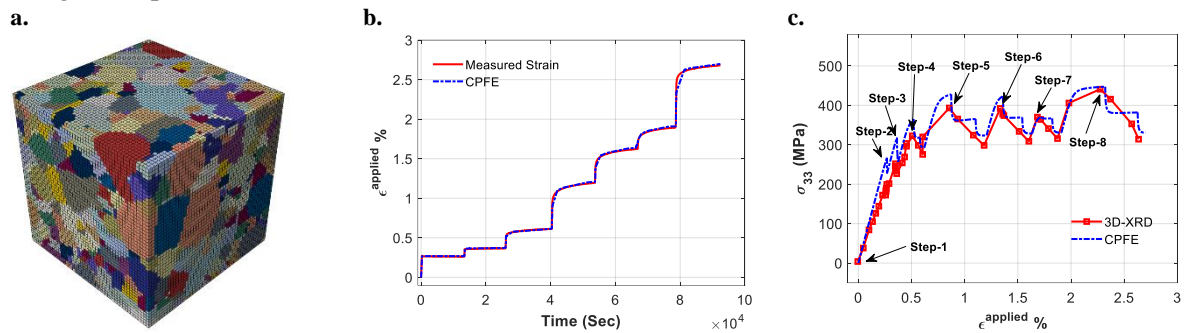

Fig. 2. (a) The simulated microstructure imported into the finite element solver. (b) A comparison between the in-situ measured strain and the calculated strain from the model. (c) A comparison between the in-situ measured and simulated macroscopic stress strain curve.

The slip systems considered in the modelling are prismatic$\langle 11\bar{2}0 \rangle$, basal $\langle 11\bar{2}0 \rangle$, and pyramidal $\langle 11\bar{2}3 \rangle$ with the $\{10\bar{1}2\}\langle 10\bar{1}1 \rangle$ twinning system included as pseudo slip. The strain rate and hardening parameters used for each slip or twinning system are provided in Table 1. The elastic constants of zirconium single crystal were taken from Fisher and Renken [54]: C_{11}=143.5 GPa, C_{33}=164.9 GPa, C_{12}=72.5 GPa, C_{13}=65.4 GPa, and C_{44}=32.1 GPa. No twins existed in the model in the first increment, but nucleation was allowed when the relative volume fraction of a "possible" twin at an IP reached a critical value, i.e. 0.03. At this stage, the orientation of the twin was determined by reflecting the parent orientation across the twin habit plane as explained in Abdolvand et al [49]. No stress calculation was

7

done for the twinned domain and it was simply assumed that stress in the twin was equal to that of the parent.

Table 1: The single crystal properties of zirconium used in CPFE modelling [49]

	n	$\dot{\gamma}_0(s^{-1})$	g_0^α (GPa)	g_1^α (GPa)	θ_0^α (GPa)	θ_1^α (GPa)
Prism	20	3.5×10^{-4}	0.12	0.33	0.01	0
Basal	20	3.5×10^{-4}	0.168	0.22	0.05	0
Pyramidal	20	1.0×10^{-4}	0.331	0.27	0.62	0.28
Twinning	20	1.0×10^{-4}	0.25	0.2	0.05	0

4. Results

In all results presented, σ_{11}, σ_{22}, σ_{33}, represent the normal stresses measured along the beam direction, the transverse direction, and the loading direction, respectively.

4.1 General trends

The statistics of the 3D-XRD experiment for the measured volume are shown in Table 2. At the preload (Step-1), 11703 grains were indexed with an average of 119 peaks per grain. It is shown that all volume average stress components are close to zero except for σ_{33}, which increases with the macroscopic stress. The grain weighted average for σ_{33} falls in between the maximum macroscopic stress measured for each step and the one at the end of the pattern collection when the specimen is relaxed. Due to the conservative criteria imposed in the grain indexing codes and plasticity-induced peak smearing, the number of measured grains drops with increasing strain, except for the unload step (Step-9) where elastic strain and rotations are restored, and it was possible to index more grains. The average number of peaks per grain, however, is more than 97 for all steps. The measured error bar for each stress component is also provided in Table-2.

Table 2: 3D-XRD measurement steps and statistics.

Step ID	Description	Applied Strain %	Applied stress (MPa) Start*	End**	No. of grains	No. of Peaks per grain	Grain weighted average of stresses with estimated errors (MPa) σ_{11}	σ_{22}	σ_{33}	σ_{23}	σ_{13}	σ_{12}	Beam height (μm)
1	Step-1	0.001	8	8	11703	119	-4.0 ±17.5	0.3 ±13.3	1.6 ±11.4	-0.1 ±3.2	0.3 ±3.4	-1.0 ±4.3	40
2	Step-2	0.257	180	172	11308	118	-6.3 ±16.8	-6.2 ±12.6	169.4 ±10.8	0.2 ±3.1	1.4 ±3.3	-1.4 ±4.1	
3	Step-3	0.355	233	226	11087	117	-4.4 ±15.9	2.6 ±11.2	227.1 ±10.3	0.7 ±2.9	1.5 ±3.11	-1.4 ±4.0	
4	Step-4	0.565	297	274	10995	115	-2.8 ±15.5	1.6 ±11.7	287.1 ±10.0	0.9 ±2.8	1.3 ±3.03	-1.6 ±3.9	
5	Step-5	1.087	321	295	10578	109	-2.1 ±21.0	-1.8 ±15.7	301.3 ±13.5	1.1 ±3.9	0.6 ±4.1	-1.5 ±5.2	
6	Step-6	1.524	329	304	9071	105	5.9 ±26.6	1.1 ±19.6	315.3 ±17.0	1.7 ±4.8	0.3 ±5.2	-1.6 ±6.6	
7	Step-7	1.890	335	310	8042	102	12.7 ±29.5	5.5 ±21.7	325.6 ±18.9	0.8 ±5.4	1.3 ±5.8	-1.3 ±7.5	
8	Step-8	2.600	344	306	7312	97	20.3 ±44.0	3.1 ±32.2	327 ±28.0	2.4 ±8.0	0.3 ±8.6	-1.4 ±11.0	25
9	Step-9	2.271ˣ	2	3	8455	102	17.8 ±43.3	32.2 ±31.4	-3.9 ±27.3	0.8 ±7.6	-0.2 ±8.4	-2.7 ±10.7	

*Measured at the end of reloading; ** Measured at the end of pattern collection. ˣMeasured strain at unload

In Fig. 3. the propensity of the misorientation between the HCP crystals c-axis and the beam direction (β) for different steps are shown. The specimen was cut so that HCP crystals have their c-axis both along the LD and TD so that with loading, a combination of both twinned and un-twinned grains can be studied. The twinned grains are mainly the "hard" grains with their c-axis along the LD and since tensile twinning results in 85° reorientation, twins will appear along both TD and BD. In the undeformed specimen, only a few grains had their c-axis along BD (see Table 3), hence, we plot the propensities with respect to BD to avoid mixing parents with twins. For each step, propensities are determined by

8

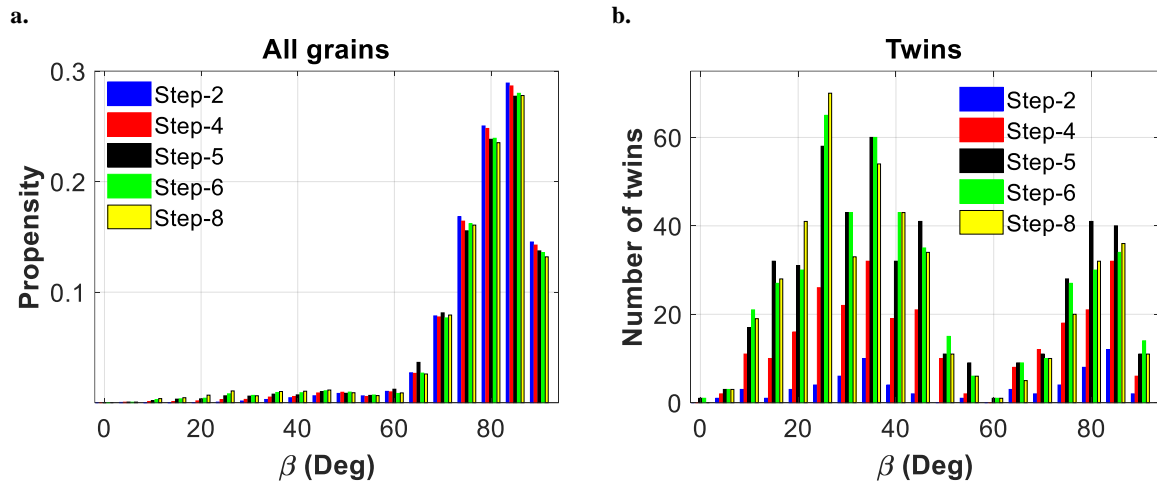the number of grains measured for a given β range to the total number of grains indexed for the same step.

Fig. 3. The distribution of β for (a) all grains and (b) only twins, at different measurement steps. β is the rotation angle between the HCP crystal c-axis and the beam direction.

In Fig. 3a, the propensity of β for all grains is shown. It can be seen that, while the propensity of grains with $\beta > 75°$ decreases, that of grains with $\beta < 25°$ increases. This shows that twins form with tensile loading, where a fraction of parent grains transforms into twins. Since β for twins spread from 0° to 90°, i.e. from BD to TD, the propensity of twins is overshadowed by those from parents. Hence, the number of twins as a function of β is plotted in Fig. 3b. In this figure, only the twins that were successfully matched with parent grains are shown. It can be seen that in Step-2 only a few twins exist, but with further loading, the number of twins increases where a peak is observed at $\beta = 25°$. At the early stages of plasticity, a rapid growth in the number of twins is observed, e.g in steps 3, 4, and 5, but the number of captured twins has relatively stayed the same for steps further into the plasticity zone, e.g., steps 6, 7, and 8.

Table. 3. Results from twin-parent matching process

Step	Number of grains with $\beta < 30°$	Number of grains with $\beta < 40°$	Number of matched pairs
Step-1	7	53	16
Step-2	18	82	80
Step-3	34	100	113
Step-4	87	189	282
Step-5	187	341	499
Step-6	196	354	506
Step-7	181	303	410
Step-8	212	348	492
Step-9	255	431	591

The number of captured twins from the developed matching method is provided in Table 3. In order to confirm the validity of this method, the number of matched twins is compared with the total number of grains with β less than 30° and 40°. This can be considered as a "validation" test for the developed matching method as β was not used for defining a twin or a pair. In Table-3, it is shown that it was possible to track 16 pairs back to Step-1. We believe that these pairs formed during polishing of the specimen. This number falls in between 7 and 53 grains that have their β less than 30° and 40°. It is worth mentioning that twins form with their c-axis both along BD and TD and the numbers presented in the second and third columns of Table 3 only show a fraction of twins, not all of them. Nevertheless, the observed trends are consistent from the two methods; for example, the number of twins jumps in Steps 3, 4, and 5 and stays unchanged in step 6, 7, and 8. The reduction observed in Step-7 is due to plasticity and significant peak smearing that reduces the number of indexed grains; however, due to

reducing the X-ray beam height in the subsequent step (Step-8), a better grain indexing rate was achieved and the number of pairs returned close to what it was in Step-6.

In order to determine the smallest twin size indexed in this experiment, the measured relative volumes for twin-parent pairs are used. Grain size for parent grains is defined as grain diameter assuming that grains are spherical and space filling. Since twins are lenticular, if we assume that they cut through their parent grain, their thickness can be determined as $t_T = \frac{4V_T}{\pi D_P{}^2}$, where V_T is the volume of the twin from peak analysis, and D_P is the diameter of its corresponding parent grain. With the use of this analysis, the thickness of the smallest twins at Step-2 and Step-3 are 0.051 μm and 0.059 μm respectively. If these twins were assumed to be spherical, their diameters would respectively be 11.5 μm and 14.3 μm.

The distribution of σ_{33} and evolution of texture are shown in Fig. 4. The results shown in Fig. 4a-4h are the (0002) pole figures from 3D-XRD, where each circle represents a grain, with the colour being proportional to the measured σ_{33} and the size being proportional to the measured relative volume for the grain. Similarly, the results for the modelled grains are shown in Fig. 4i-4l. To better show the variations, the limits of the colour bars are rescaled for each of the sub-figures. It is shown that, at the preload, crystals with their c-axis oriented towards the LD generally have tensile σ_{33}, whereas those oriented towards TD have compressive σ_{33}. These are the residual stresses that developed during the heat treatment. The trends observed in the experiment at the preload are consistent with those calculated with CPFE considering thermal contraction during cooling as shown in Fig. 4i. Further, in section 5.2, it is shown that the tensile residual σ_{33} observed in some grains will promote nucleation of twins as early as Step-2, before the onset of macroscopic plasticity. In Fig. 4b the measured poles at Step-2 are shown. The poles located towards TD are elastically and plastically "soft" grains that exhibit low stresses. This is further captured in the CPFE modelling as shown in Fig. 4j. In Fig. 4c, new poles are observed at ~25° from the BD, which are also observed in the results of CPFE modelling (Fig. 4k) confirming the nucleation of twins at the onset of macroscopic plasticity. The stresses calculated with CPFE are slightly higher, consistent with the simulated macroscopic response. This is due to the assumption that stress within the twin is equal to that of the parent and underestimating the effects of the twin transformation strain. Specifically, the constitutive model, which uses a pseudo-slip formulation, does not explicitly consider twinned domains. It therefore does not allow evaluating how stresses are partitioned between parent and twinned domains. A rapid increase in the number of new poles is observed in Fig. 4d and 4e reflecting formation of more new twins. The same trend is observed in the results of CPFE where new poles are clearly formed close to TD with many others at ~25° from the BD. In steps 6 to 8, the distributions of σ_{33} and (0002) poles do not change significantly (Fig. 4f-4h). This is also reflected in the macroscopic stress-strain curve where almost no hardening is observed between these steps.
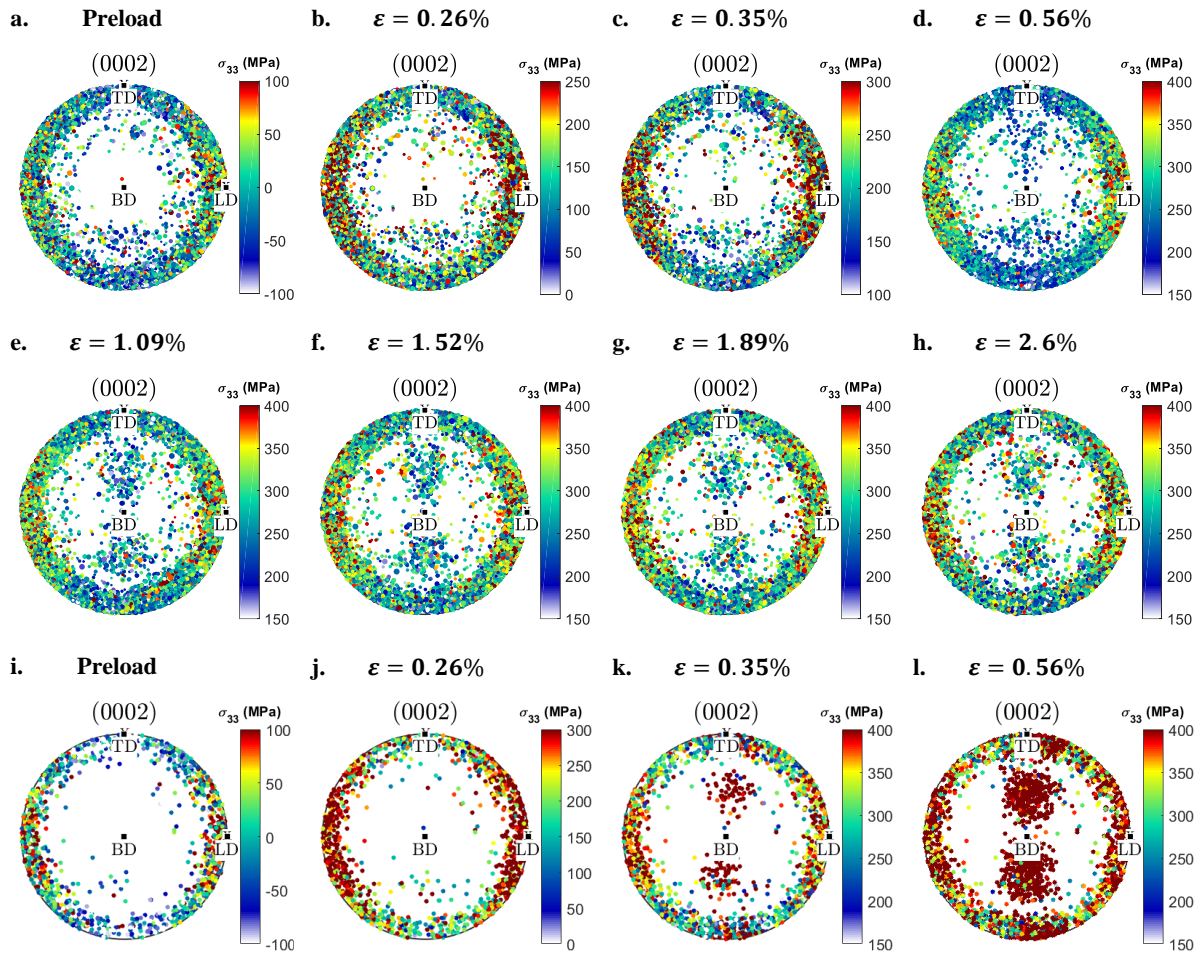
Fig. 4. The evolution of texture and stress for individual grains. 3D-XRD (**0002**) pole figures for (a) Step-1, (b) Step-2, (c) Step-3, (d) Step-4, (e) Step-5, (f) Step-6, (g) Step-7, and (h) Step-8. CPFE results for (i) Step-1, (j) Step-2, (k) Step-3, (l) Step-4. Each circle represents a grain where the colour of the circle is proportional to the measured or calculated stress along the loading direction (σ_{33}), as shown in the colour bar in the right-hand side of the figure. In (a) to (h) the size of the circles is proportional to the measured relative volume of the grain.

11

4.2 Twin-parent pairs: early stages of plasticity

The development of stress in the matched twin-parent pairs is shown in Fig. 5. Only steps 3 to 5 are discussed in this section, i.e., the nucleation steps at which a jump in the number of twins is observed. In Fig. 5a, the measured axial stress σ_{33} of twins at Step-3 is plotted as a function of that of the corresponding parents. The blue circles represent the pairs while the red dot represents the average value calculated for all pairs. The black dashed lines are to bisect the figures and highlights when the quantity of the vertical axis is equal to that of the horizontal axis. It can be seen that, on average, twins are generally less stressed than their parents, although some twins develop higher σ_{33} than their parents. The measured σ_{33} in twin and parent pairs for steps 4 and 5 are respectively shown in Fig 5b and 5c. While more twin and parent pairs are captured, on average twins are generally less stressed. However, with applying more strain, the red dots are distancing from the dashed black line. That is, σ_{33} in twins is closer to their corresponding parents, and twins are more stressed in Step-3 than Step 4 and 5.

Unlike σ_{33}, the stresses in the TD (σ_{22}) and BD (σ_{11}) within twins are higher than their corresponding parents (see Figs. 5d and 5e). These two stress components are only provided for Step-3, but the observed trends hold for the rest of the steps. For example, while the average σ_{22} and σ_{11} for parent grains are nearly zero, the corresponding values for twins are positive and moderately increasing from Step-3 to Step-5 (Fig. 5f).

With the method developed for matching twin-parent pairs it was possible to determine which one of the six variants of $\{10\bar{1}2\}\langle10\bar{1}1\rangle$ twinning system was active. Once the active variant was determined, it was possible to rotate the measured stress tensor to the twin coordinate system. In Figs. 5g to 5i, σ_{Normal}^{Twin} and σ_{Normal}^{Parent} represent the stresses normal to the twin habit plane calculated using the measured stresses within the twin and parent, respectively. Likewise, in Figs. 5j to 5l, τ_{RS}^{Twin} and τ_{RS}^{Parent} represent the shear stress calculated on the twin habit plane in the twinning direction using the measured stresses within the twin and parent, respectively. In all figures, the normal to the habit plane and shear direction from the *parent* grain is used to project stresses into a given direction. A nearly "perfect" linear relationship between σ_{Normal}^{Twin} and σ_{Normal}^{Parent} is observed which holds for all measurement steps. For example, the average of σ_{Normal}^{Parent} at Step-3 is 121.3 MPs while that of σ_{Normal}^{Twin} is 119.9 MPa. With increasing the applied strain and proceeding to Step-4, this average for parents and twins is respectively, 135.8 MPa and 127.9 MPa. In all measurement steps, σ_{normal} for both twin and parent grains is positive and varies between 50 MPa and 300 MPa.

It is shown in Fig. 5j that while the resolved shear stress within both twin and parent is positive, τ_{RS}^{Parent} is two times higher than τ_{RS}^{Twin}. Proceeding to Step-4 and Step-5, a wider distribution of τ_{RS} within the parent grains is observed, but not so within the twins. This suggests that, at the early stages of plasticity, parent grains undergo more plastic deformation than the twins, and since twins are thin, they deform mainly elastically. In addition, on average, τ_{RS} in both twin and parent grains increases with increasing the applied stress. To better visualize the state of τ_{RS} within the captured twin-parent pairs at Step-5, a 3D plot of the pairs is shown in Fig. 6a.
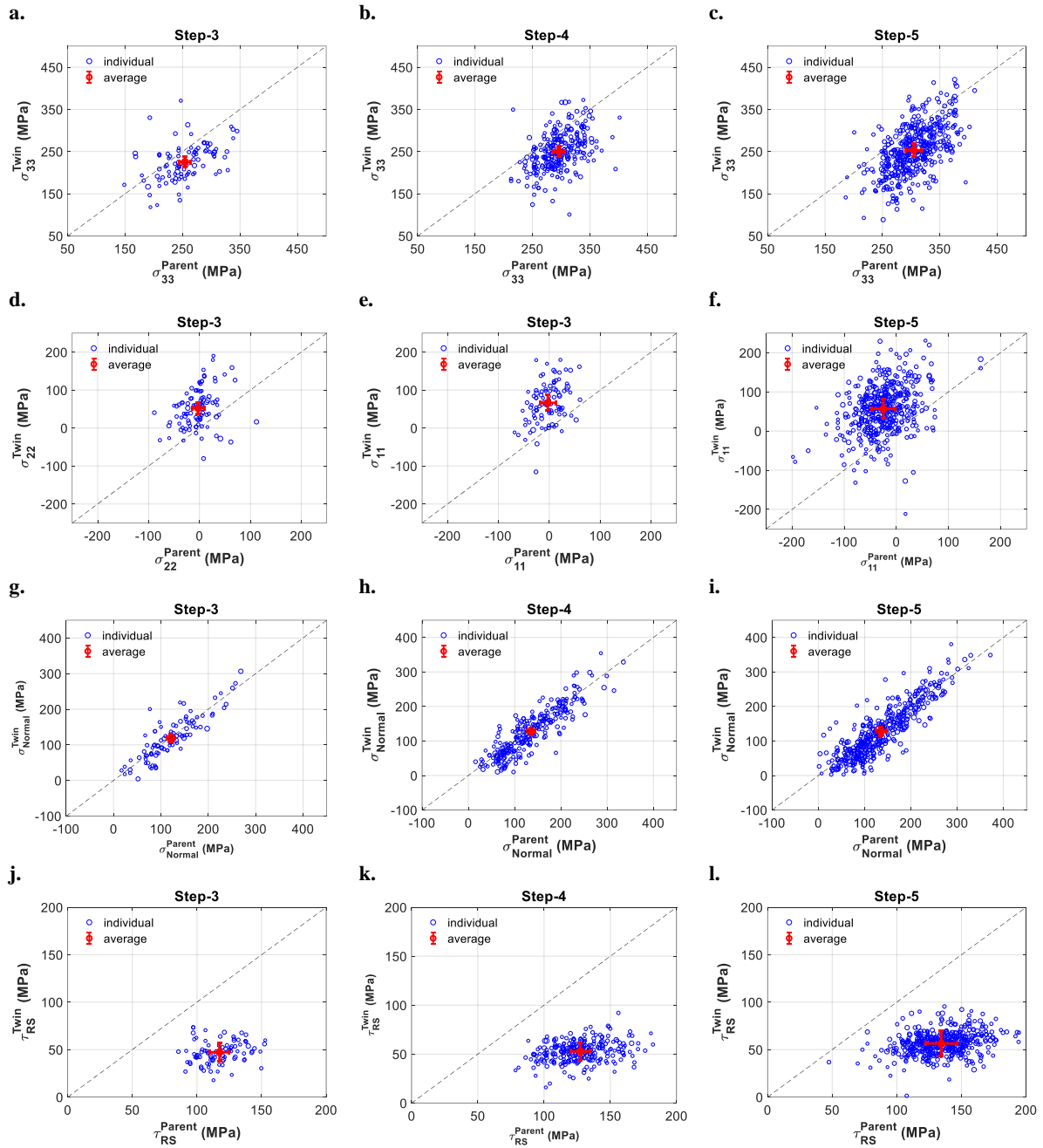
Fig. 5. Stress in the twin as a function of stress in the corresponding parent: σ_{33} at (a) Step-3, (b) Step-4, and (c) Step-5; σ_{22} at (d) Step-3, and σ_{11} at (e) Step-3, and (f) Step-5; σ_{Normal} at (g) Step-3, (h) Step-4 and (i) Step-5; τ_{RS} at (j) Step-3, (k) Step-4, and (l) Step-5. σ_{Normal} and τ_{RS} are the normal and shear stresses acting on the twin habit plane and in the twin direction, respectively. The dashed back lines are to bisect the figures and indicate when the quantity of the vertical axis is equal to that of the horizontal axis. Red crosses are the average values for each population with their corresponding average error bars.

The populations of twins for the extracted twin variants in steps 3 and 4 are shown in Fig. 6b and 6c. To calculate the twin local Schmid factor (SF), the measured stress tensor within the parent (σ^{Parent}) in the step prior to detecting the twin was substituted into $SF = \frac{P^{\alpha}:\sigma^{Parent}}{\|\sigma^{Parent}\|}$, where the denominator represents the norm of stress tensor and P^{α} is the symmetric part of the Schmid tensor for the active variant [55]. The same equation is used for calculating the global SF, but the applied stress was used instead of the grain resolved stress tensor. Once the SFs for all six twin variants were calculated, they

13

were sorted from the highest to the lowest and the rank of the twin variant was determined. The rank of the twinned variants for global and local SFs was determined independently.

In Figs 6b and 6c, it is shown that all twin variants are active, but the first three variants are more frequent, regardless of using global or local stresses in determining SFs. The twins captured in Step-3 are generally from the parent grains with their c-axis nearly parallel to the LD and hence, all of the six twin variants are equally active. However, with the use of the local stress for calculating SFs, a better estimation of the active variants is obtained since the frequency of the strongest variants is higher. With proceeding to Step-4, similar trends are observed for the distribution of twin variants using local and global SFs.
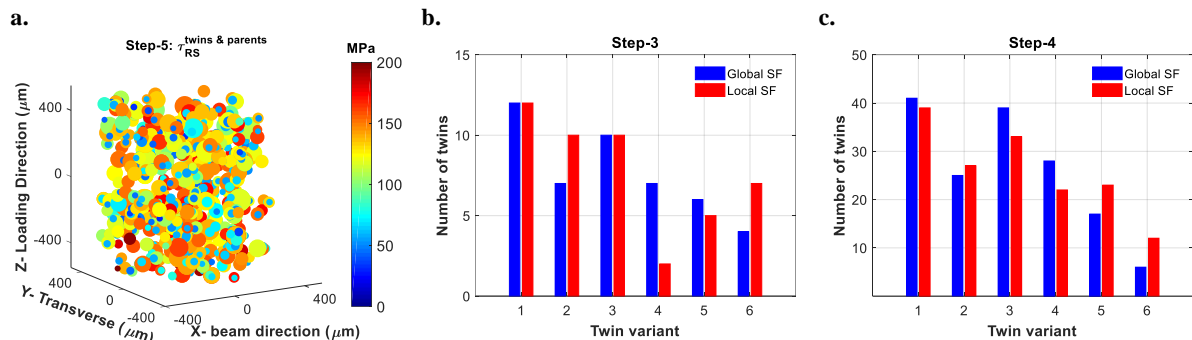

Fig. 6. (a) a 3D view of twin-parent pairs captured in Setp-5. The size of the spheres is proportional to the measured relative volumes and colours are proportional to the measured resolved shear stresses on the twin habit planes. The number of twins for a given twin variant at (b) Step-3 and (c) Step-4. In (b) and (c) Global SF and local SF represent the Schmid factors calculated using the measured global or local stresses and twin variants are ordered from highest to the lowest.

14

4.3 Twin-parent pairs: plasticity

Between Step-6 and Step-8, the macroscopic strain varies from 1.52% to 2.6 % while the macroscopic axial stress remains quasi-constant, which corresponds to the absence of work hardening. The development of stresses in twin-parent pairs for steps 6 to 8 are shown in Fig. 7. It is shown that, similar to steps 3 to 5, the axial stress σ_{33} in twins is generally less than that of parents (Figs. 7a to 7c). Due to the absence of work hardening, the average values (red dots) for the stress components σ_{33}, σ_{22} and σ_{11} do not change significantly between steps 6 and 8.

The normal stresses (σ_{Normal}) acting on the twin habit plane for steps 6 to 8 are shown in Figs. 7d to 7f. Results are consistent with those measured in steps 3 to 8 where a linear relationship between σ_{Normal} within parents and twins is captured. In all cases σ_{Normal} is positive and varies between 50 MPa to 350 MPa, a slightly broader range than that measured for steps 3 to 5. τ_{RS} measured in twin-parent pairs for steps 6 to 8 are shown in Figs 7g to 7i. Consistent with previous results, τ_{RS} within parents are higher than $2\tau_{RS}^{Twin}$. Also, with further loading from Step-6 to Step-8, the distribution of τ_{RS} for parents further broadens, whereas for twins not much broadening is observed. This is also reflected in the calculated average error bars and indicates that twin and parent grains accommodate the applied strain at different rates.
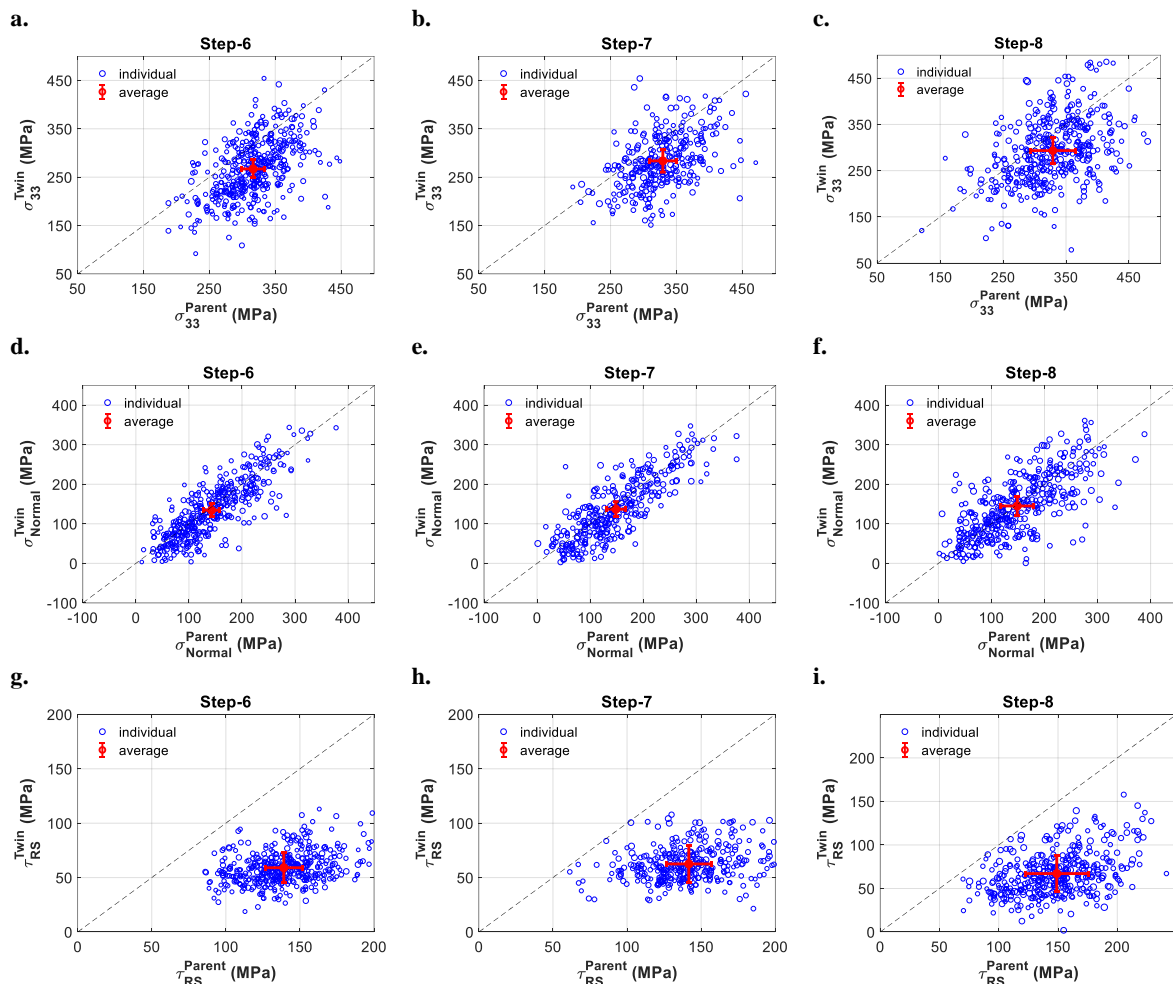

Fig. 7. Stress in the twin as a function of stress in the corresponding parent: σ_{33} at (a) Step-6, (b) Step-7, and (c) Step-8; σ_{Normal} at (d) Step-6, (e) Step-7 and (f) Step-8; τ_{RS} at (g) Step-6, (h) Step-7, and (i) Step-8. σ_{Normal} and τ_{RS} are the normal and shear stresses acting on the twin habit plane and in the twin direction, respectively. The dashed back lines are to bisect the figures and indicate when the quantity of the vertical axis become equal to that of the horizontal axis. Red crosses are the average values for each population with their corresponding average error bars.

15

4.4 Twin-parent pairs: Unload

After deforming the specimen to 2.6% strain, the specimen was unloaded to nearly zero applied stress at the unload step (Step-9). The measured (0002) pole figure for all grains measured at Step-9 is shown in Fig 8a. The range of σ_{33} at unload is similar to that of preload, i.e. -150 MPa to 150 MPa, but a less distinct variation of σ_{33} from TD to LD is observed at the unload step. This means that after deforming the specimen to 2.6% applied strain, the effects of thermal residual stresses disappear. In addition, at unload, the grains located at TD are slightly in compression while those located at LD are in tension. This follows the trends observed at Step-8 where the soft grains with their crystal c-axis pointing towards TD are less stressed than hard grains (Fig. 4h).

The stress state within twin-parent pairs at unload is shown in Fig. 8b-8d. It is shown that upon unloading, the average of σ_{33} for both twins and parent grains is nearly zero (Fig. 8b) while σ_{Normal} in twins is still linearly correlated to that of the corresponding parents (Fig. 8c). At unload, unlike the other 7 steps, σ_{Normal} is not systematically positive and varies between -100 MPa to 100 MPa. Interestingly, while the average of τ_{RS} in the twins is -36.9 MPa, that in parent grains is positive and is 6.8 MPa (Fig. 8d). An important conclusion that can be drawn from these data is that τ_{RS} in both twin and parent can be negative while the twin is still not annihilated.
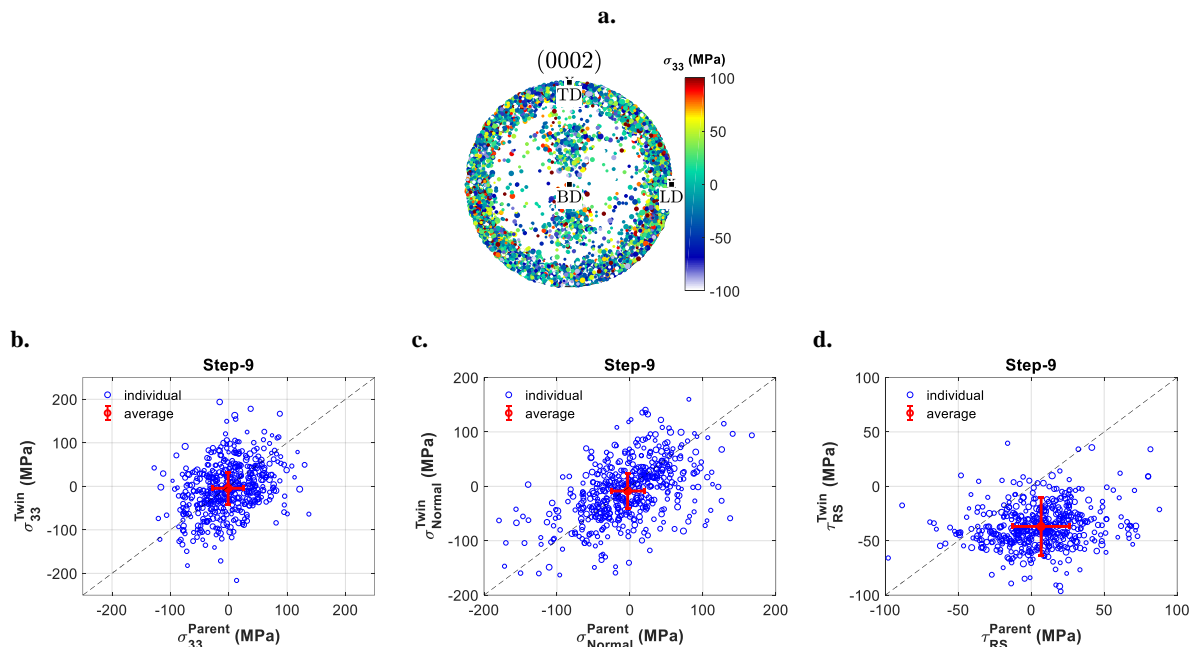

Fig. 8. 3D-XRD results for unload (Step-9): (a) (0002) pole figure; stress in the twin as a function of stress in the corresponding parent (b) σ_{33}, (c) σ_{Normal}, and (d) τ_{RS}. The color of each pole in (a) is proportional to the measured σ_{33} and the size of the pole is proportional to the measured relative volume.

5. Discussion

5.1 General discussion

So far the state of stress within twin and parent pairs of each step is studied independently from other steps and from CPFE results. The stress-strain curve for all twin-parent pairs measured in the 3D-XRD experiment is shown in Fig. 9a. The blue and black lines represent individual parent and twin grains, respectively, while the green and red line respectively represent the average stress measured for parents and twins. In section 4.2, it was shown that σ_{33} within twins at Step-3 is close that in parents, but with proceeding to step 5, the difference between the stresses increases and twins relax. In Fig 9a, it is shown that the red line nearly coincides with the green line at Step-3. This could be due to a size effect, i.e. that twins of Step-3 are smaller than those in steps 4 and 5 and hence are harder. To further investigate

16

this aspect, the state of stress for the 64 twins that were captured in Step-2 is studied. These 64 twins are the ones that nucleated in the hard grains with positive thermal residual stresses that helped nucleation of twins in Step-2. The average stress for all twins of each step are calculated and reduced from those from the parents and results are provided in Table 4. It can be seen that the difference between σ_{33} of the pairs increases from Step-3 to Step-5. While this difference at Step-3 is 28.5 MPa, at Step-2 is only 16 MPa indicating that twins are not much relaxed at the early stages of plasticity. Similarly, the difference between the resolved shear stress within twin and parent in Step-2 is minimum yet increases with further loading and increasing to Step-5. This observation supports the previous numerical studies that concluded that directional Hall-Petch effects [56], as well as non-local effects [46] should be incorporated into modelling of twins. In addition, it suggests that twin and parent grains accommodate the applied strain at different rates.
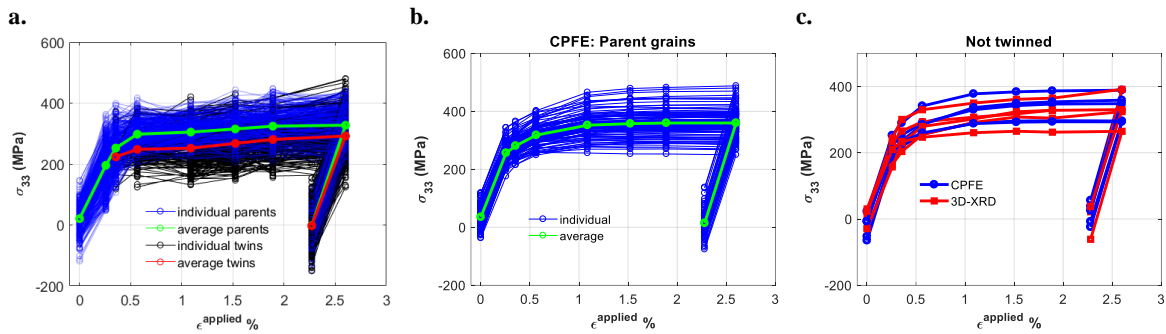

Fig. 9. (a) The measured stress-strain curve for twin-parent pairs from 3D-XRD. The green and red lines represent the average values for each population. (b) CPFE results for paent grains. (c) Comparison between CPFE and 3D-XRD results for the grain that did not twin. In all sub-figures strains on the horizontal axis are the macroscopic applied strains.

Proceeding further into the plasticity zone, no significant changes in the difference between measured σ_{33} of twins and parents is observed in steps 5 to 8 (Table 4). Interestingly, σ_{Normal} in all steps, including unload, stays the same in parents and twins. The CPFE results for the stress-strain curve for all parent grains are shown in Fig. 9b. Results are for the average stresses calculated from all IPs assigned to each grain so that a like-to-like comparison can be made and data are extracted at the end of each measurement step. Generally, a good agreement with experimental results is achieved for the average response of the cluster of modelled parent grains. The stress-strain curve for some of the grains that did not twin in the experiment and model are plotted in Fig. 9c. This figure shows that in the absence of twinning, a good agreement can be achieved at the grain level, however, the current constitutive equation should be modified to capture a better response for the twinned grains (see below).

Table 4. The average difference between measured stresses in twins and parents

Step	$\sigma_{33}^{Pa} - \sigma_{33}^{Tw}$ (MPa)	$\sigma_{Normal}^{Pa} - \sigma_{Normal}^{Tw}$ (MPa)	$\tau_{Rs}^{Pa} - \tau_{Rs}^{Tw}$ (MPa)
Step-2	16	1.4	62.7
Step-3	28.5	1.4	70.2
Step-4	46	7.9	74.6
Step-5	51.3	7.8	78.0
Step-6	49.4	8.2	80.0
Step-7	45.7	11.5	79.1
Step-8	35.8	3.6	81.8
Step-9	3.5	5.5	43.6

5.2 Stress development: individual pairs

In this section, the behaviour of individual twin-parent pairs is studied to understand the origin of the trends reported in the previous sections for the average behaviour of the pairs. In Fig. 10, the measured stress-strain curves for several twin-parent pairs are provided. For these pairs, the parent grains were imported into CPFE model and it was possible to track them back to Step-1. Only the steps that the pairs were indexed, matched, and tracked with high confidence are shown. Modelling results for each step are the average σ_{33} calculated from all IPs assigned to the parent.
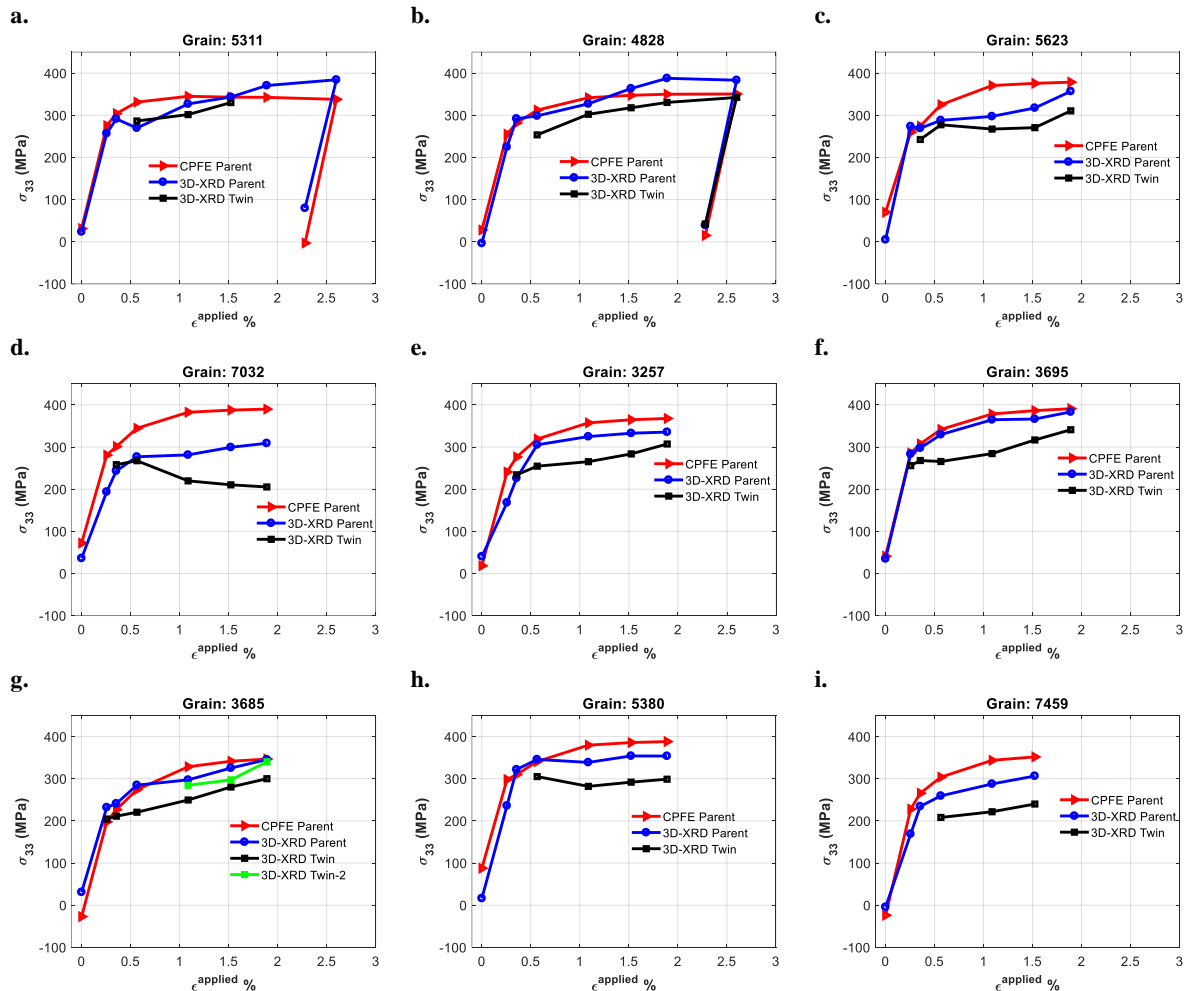

Fig. 10. Stress-strain curve for individual twin-parent pairs. Parent IDs are provided in the titles of figures, and IDs are generated during grain indexing. Blue curves represent 3D-XRD results for parents, black and green curves represent 3D-XRD results for twins, and red curves represent CPFE results for parent grains. In all sub-figures strains on the horizontal axis are the macroscopic applied strains.

In Figs. 10a to 10c, a twin was captured in Step-3 where in all cases, a distinct drop in the stress of the parent is observed. This means that upon nucleation of twins, a discernible relaxation takes place within the parent grain which is not observed in any of the CPFE results. The stress relaxation is due to twin transformation strain that is underestimated in the current constitutive equations. This stress relaxation in combination with the hard behaviour of twins at the nucleation step, due to their small sizes, are the reasons for the high stress measured for the twin of the grain 5311 (Fig. 10a). A similar trend is observed in grain 4828 and 5623 (Figs. 10c and 10d), where σ_{33} in the parent is relaxed at the nucleation step, but σ_{33} in twins in steps 3 and 4 are close to those of their corresponding parents. With further loading, the difference between the stress of twin and parent increases. In addition, two more pairs are shown in Figs. 10d and 10e, where in both cases, σ_{33} of the twin coincides with that of the corresponding parent

18

at the nucleation step, but similar to the previous cases, the difference between the two increases with further loading.

In Figs. 10f and 10g, a twin was captured as early as Step-2 where in both cases, σ_{33} of twins are nearly equal to those of their corresponding parents. It can be seen that both parent grains had tensile thermal residual stresses at the preload step, which promoted nucleation of twins in Step-2. Further, with the matching method that was developed in this paper, it was possible to capture multiple twins for a single parent as shown in Fig 10g. Two distinct stress relaxation events are observed in the grain 3685 (Fig. 10g); the first in Step-3 after the nucleation of the first twin and the second in Step-5, upon nucleation of the second twin. Interestingly, the stress in the second twin is also very close to that of parent confirming that twins at nucleation are not very much relaxed.

In Figs. 10h and 10i, two pairs are shown where the twins were captured in Step-4 and were relaxed. In the parent grain 5380 (Fig. 10h), a stress relaxation is observed in Step-5 which is due to twinning. The difference between the measured σ_{33} for twin and parent is minimum in Step-4, but increases with further loading. This is also observed in grain 7459 (Fig. 10i).

In all results presented in this paper, the measured and simulated stresses are the average values for twins or parents. The state of the stress within a twin can vary significantly particularly close to twin tips and boundary [57,58]. Likewise, stress within the parent grain can significantly vary close to twin boundaries. In section 4.4, we showed that upon unloading, τ_{RS} within twins and parents can be negative while the twin is not yet annihilated. Higher resolution experimental techniques as well as numerical modelling are required to further study the stress field in the vicinity of twins.

6. Conclusions

A three-dimensional synchrotron X-ray diffraction experiment was conducted on a pure zirconium specimen to study the evolution of stress in twin-parent pairs. The measurement was conducted during an *in-situ* uniaxial tensile experiment and in nine steps: preload, one step in the elastic zone but close to onset of plasticity, three steps that covered the onset of plasticity, three more steps in the plastic zone, and finally at unload. The measured microstructure was imported into a crystal plasticity finite element model to simulate deformation of individual grains. A new method was developed to match the newly nucleated twins with their corresponding parents and track them over different loading steps. It is shown that

(1) The difference between the stress along the loading direction (σ_{33}) measured for twins and parents is at minimum at the early stages of plasticity but increases with more plastic deformation.

(2) Twins are generally not relaxed, rather stressed in the first step that they are captured. Relaxation due to plasticity takes place within twins with further loading, but at a different rate relative to their corresponding parent grains.

(3) The other two normal stress components, σ_{11} and σ_{22}, in the twins are slightly higher than their corresponding parents.

(4) A distinct relaxation is observed in the stress-strain curve of the parent grains at the twin nucleation step.

(5) The normal stress acting on the twin habit plane (σ_{Normal}) is similar for both parent and twin grains.

(6) When twins are nucleated with their c-axis perpendicular to the tensile loading direction, the resolved shear stress acting on the twin plane in the twinning direction (τ_{RS}) within the twin is less than half of the τ_{RS} measured in the corresponding parent grain.

19

(7) For a subset of twin-parent pairs, τ_{RS} at the unload was negative in both twin and parent grains while the twin was not annihilated.

(8) The tensile thermal residual stresses within parent grains promote nucleation of twins as early as the beginning of the onset of plasticity.

(9) Thermal residual stresses in zirconium disappear with unloading from 2.6% applied strain.

(10) The first three twin variants with higher Schmid factors are the most active ones, regardless of using the local measured stress tensor or the applied stress in determining Schmid factors. A better estimation of the active variants is obtained at the early stages of plasticity with the use of the local stresses for calculating Schmid factors.

(11) With the method developed here, it was possible to capture multiple twins per parent. It is shown that the evolution of stress within the second twin follows the trends reported, i.e. stressed at nucleation but relaxed with loading.

Acknowledgment

References

[1] C.C. AydIner, J. V. Bernier, B. Clausen, U. Lienert, C.N. Tomé, D.W. Brown, Evolution of stress in individual grains and twins in a magnesium alloy aggregate, Phys. Rev. B - Condens. Matter Mater. Phys. 80 (2009) 1–6. https://doi.org/10.1103/PhysRevB.80.024113.

[2] L. Balogh, S.R. Niezgoda, A.K. Kanjarla, D.W. Brown, B. Clausen, W. Liu, C.N. Tomé, Spatially resolved in situ strain measurements from an interior twinned grain in bulk polycrystalline AZ31 alloy, Acta Mater. 61 (2013) 3612–3620. https://doi.org/10.1016/j.actamat.2013.02.048.

[3] J. Oddershede, B. Camin, S. Schmidt, L.P. Mikkelsen, H.O. Sørensen, U. Lienert, H.F. Poulsen, W. Reimers, Measuring the stress field around an evolving crack in tensile deformed Mg AZ31 using three-dimensional X-ray diffraction, Acta Mater. 60 (2012) 3570–3580. https://doi.org/10.1016/j.actamat.2012.02.054.

[4] J. Lind, S.F. Li, R. Pokharel, U. Lienert, A.D. Rollett, R.M. Suter, Tensile twin nucleation events coupled to neighboring slip observed in three dimensions, Acta Mater. 76 (2014) 213–220. https://doi.org/10.1016/j.actamat.2014.04.050.

[5] T.R. Bieler, L. Wang, A.J. Beaudoin, P. Kenesei, U. Lienert, In situ characterization of twin nucleation in pure Ti using 3D-XRD, Metall. Mater. Trans. A Phys. Metall. Mater. Sci. 45 (2014) 109–122. https://doi.org/10.1007/s11661-013-2082-3.

[6] H. Zhang, A. Jérusalem, E. Salvati, C. Papadaki, K.S. Fong, X. Song, A.M. Korsunsky, Multi-scale mechanisms of twinning-detwinning in magnesium alloy AZ31B simulated by crystal plasticity modeling and validated via in situ synchrotron XRD and in situ SEM-EBSD, Int. J. Plast. 119 (2019) 43–56. https://doi.org/10.1016/j.ijplas.2019.02.018.

[7] S.R. Agnew, A. Singh, C.A. Calhoun, R.P. Mulay, J.J. Bhattacharyya, H. Somekawa, T. Mukai, B. Clausen, P.D. Wu, In-situ neutron diffraction of a quasicrystal-containing Mg alloy interpreted using a new polycrystal plasticity model of hardening due to {10.2} tensile twinning, Int. J. Plast. 100 (2018) 34–51. https://doi.org/10.1016/j.ijplas.2017.09.005.

[8] J.C. Schuren, P.A. Shade, J. V. Bernier, S.F. Li, B. Blank, J. Lind, P. Kenesei, U. Lienert, R.M. Suter, T.J. Turner, D.M. Dimiduk, J. Almer, New opportunities for quantitative tracking of polycrystal responses in three dimensions, Curr. Opin. Solid State Mater. Sci. 19 (2015) 235–244. https://doi.org/10.1016/j.cossms.2014.11.003.

[9] D. Naragani, M.D. Sangid, P.A. Shade, J.C. Schuren, H. Sharma, J. Park, P. Kenesei, J. V Bernier, T.J. Turner, I. Parr, Investigation of fatigue crack initiation from a non-metallic inclusion via high energy x-ray diffraction microscopy, Acta Mater. 137 (2017) 71–84.

[10] W. Wu, S.Y. Lee, A.M. Paradowska, Y. Gao, P.K. Liaw, Twinning-detwinning behavior during fatigue-crack propagation in a wrought magnesium alloy AZ31B, Mater. Sci. Eng. A. 556 (2012) 278–286. https://doi.org/10.1016/j.msea.2012.06.088.

[11] L. Wu, S.R. Agnew, D.W. Brown, G.M. Stoica, B. Clausen, A. Jain, D.E. Fielden, P.K. Liaw, Internal stress relaxation and load redistribution during the twinning-detwinning-dominated cyclic deformation of a wrought magnesium alloy, ZK60A, Acta Mater. 56 (2008) 3699–3707. https://doi.org/10.1016/j.actamat.2008.04.006.

[12] W. Wu, K. An, L. Huang, S.Y. Lee, P.K. Liaw, Deformation dynamics study of a wrought magnesium alloy by real-time in situ neutron diffraction, Scr. Mater. 69 (2013) 358–361. https://doi.org/10.1016/j.scriptamat.2013.05.008.

[13] W. Wu, Y. Gao, N. Li, C.M. Parish, W. Liu, P.K. Liaw, K. An, Intragranular twinning, detwinning, and twinning-like lattice reorientation in magnesium alloys, Acta Mater. 121 (2016) 15–23. https://doi.org/10.1016/j.actamat.2016.08.058.

[14]   M. Arul Kumar, B. Clausen, L. Capolungo, R.J. McCabe, W. Liu, J.Z. Tischler, C.N. Tomé, Deformation twinning and grain partitioning in a hexagonal close-packed magnesium alloy, Nat. Commun. 9 (2018) 4761. https://doi.org/10.1038/s41467-018-07028-w.

[15]   M. Lentz, R.S. Coelho, B. Camin, C. Fahrenson, N. Schaefer, S. Selve, T. Link, I.J. Beyerlein, W. Reimers, In-situ, ex-situ EBSD and (HR-)TEM analyses of primary, secondary and tertiary twin development in an Mg-4wt%Li alloy, Mater. Sci. Eng. A. 610 (2014) 54–64. https://doi.org/10.1016/j.msea.2014.05.025.

[16]   L. Capolungo, P.E. Marshall, R.J. McCabe, I.J. Beyerlein, C.N. Tomé, Nucleation and growth of twins in Zr: A statistical study, Acta Mater. 57 (2009) 6047–6056. https://doi.org/10.1016/j.actamat.2009.08.030.

[17]   J. Jiang, T. Ben Britton, A.J. Wilkinson, The orientation and strain dependence of dislocation structure evolution in monotonically deformed polycrystalline copper, Int. J. Plast. 69 (2015) 102–117. https://doi.org/10.1016/j.ijplas.2015.02.005.

[18]   M.R. Barnett, A. Ghaderi, J. Quinta Da Fonseca, J.D. Robson, Influence of orientation on twin nucleation and growth at low strains in a magnesium alloy, Acta Mater. 80 (2014) 380–391. https://doi.org/10.1016/j.actamat.2014.07.013.

[19]   H. Abdolvand, A.J. Wilkinson, Assessment of residual stress fields at deformation twin tips and the surrounding environments, Acta Mater. 105 (2016) 219–231. https://doi.org/10.1016/j.actamat.2015.11.036.

[20]   Y. Guo, J. Schwiedrzik, J. Michler, X. Maeder, On the nucleation and growth of $\{11\bar{2}2\}$ twin in commercial purity titanium: In situ investigation of the local stress field and dislocation density distribution, Acta Mater. 120 (2016) 292–301. https://doi.org/10.1016/j.actamat.2016.08.073.

[21]   C. Paramatmuni, F.P.E. Dunne, Effect of twin crystallographic orientation on deformation and growth in Mg alloy AZ31, Int. J. Plast. (2020). https://doi.org/https://doi.org/10.1016/j.ijplas.2020.102775.

[22]   Y. Guo, H. Abdolvand, T.B. Britton, A.J. Wilkinson, Growth of $\{11\bar{2}2\}$ twins in titanium: A combined experimental and modelling investigation of the local state of deformation, Acta Mater. 126 (2017) 221–235. https://doi.org/10.1016/j.actamat.2016.12.066.

[23]   A. Khosravani, D.T. Fullwood, B.L. Adams, T.M. Rampton, M.P. Miles, R.K. Mishra, Nucleation and propagation of $\{1\,0\,1\,\bar{2}\}$ twins in AZ31 magnesium alloy, Acta Mater. 100 (2015) 202–214. https://doi.org/10.1016/j.actamat.2015.08.024.

[24]   J.S. Chen, Y. Liu, R.J. McCabe, J. Wang, C.N. Tomé, Quantifying elastic strain near coherent twin interface in magnesium with nanometric resolution, Mater. Charact. 160 (2020) 110082. https://doi.org/10.1016/j.matchar.2019.110082.

[25]   H. Abdolvand, A.J. Wilkinson, On the effects of reorientation and shear transfer during twin formation: Comparison between high resolution electron backscatter diffraction experiments and a crystal plasticity finite element model, Int. J. Plast. 84 (2016) 160–182. https://doi.org/10.1016/j.ijplas.2016.05.006.

[26]   M. Arul Kumar, L. Capolungo, R.J. McCabe, C.N. Tomé, Characterizing the role of adjoining twins at grain boundaries in hexagonal close packed materials, Sci. Rep. 9 (2019) 1–10. https://doi.org/10.1038/s41598-019-40615-5.

[27]   M.A. Kumar, I.J. Beyerlein, R.J. Mccabe, C.N. Tome, Grain neighbour effects on twin transmission in hexagonal close-packed materials ´ 1, Nat. Commun. 7 (2016) 13826. https://doi.org/10.1038/ncomms13826.

[28]   C.N. Tomé, R. a. Lebensohn, U.F. Kocks, A model for texture development dominated by

deformation twinning: Application to zirconium alloys, Acta Metall. Mater. 39 (1991) 2667–2680. https://doi.org/10.1016/0956-7151(91)90083-D.

[29]   S.R. Agnew, D.W. Brown, C.N. Tomé, Validating a polycrystal model for the elastoplastic response of magnesium alloy AZ31 using in situ neutron diffraction, Acta Mater. 54 (2006) 4841–4852. https://doi.org/10.1016/j.actamat.2006.06.020.

[30]   O. Muránsky, D.G. Carr, M.R. Barnett, E.C. Oliver, P. Šittner, Investigation of deformation mechanisms involved in the plasticity of AZ31 Mg alloy: In situ neutron diffraction and EPSC modelling, Mater. Sci. Eng. A. 496 (2008) 14–24. https://doi.org/10.1016/j.msea.2008.07.031.

[31]   H. Wang, S.Y. Lee, E.W. Huang, J. Jain, D. Li, Y. Peng, H.S. Choi, P. Wu, Crystal plasticity modeling and neutron diffraction measurements of a magnesium AZ31B plate: Effects of plastic anisotropy and surrounding grains, J. Mech. Phys. Solids. 135 (2020) 103795. https://doi.org/10.1016/j.jmps.2019.103795.

[32]   M. Arul Kumar, A.K. Kanjarla, S.R. Niezgoda, R.A. Lebensohn, C.N. Tomé, Numerical study of the stress state of a deformation twin in magnesium, Acta Mater. 84 (2015) 349–358. https://doi.org/10.1016/j.actamat.2014.10.048.

[33]   S.R. Kalidindi, Incorporation of deformation twinning in crystal plasticity models, J. Mech. Phys. Solids. 46 (1998) 267–290. https://doi.org/10.1016/S0022-5096(97)00051-3.

[34]   a. Staroselsky, L. Anand, A constitutive model for hcp materials deforming by slip and twinning: Application to magnesium alloy AZ31B, Int. J. Plast. 19 (2003) 1843–1864. https://doi.org/10.1016/S0749-6419(03)00039-1.

[35]   T.J. Barrett, R.J. Mccabe, D.W. Brown, B. Clausen, S.C. Vogel, M. Knezevic, Predicting deformation behavior of α-uranium during tension, compression, load reversal, rolling, and sheet forming using elasto-plastic, multi-level crystal plasticity coupled with finite elements, J. Mech. Phys. Solids. 138 (2020).

[36]   N. Grilli, P. Earp, A.C.F. Cocks, J. Marrow, E. Tarleton, Characterisation of slip and twin activity using digital image correlation and crystal plasticity finite element simulation: Application to orthorhombic α-uranium, J. Mech. Phys. Solids. 135 (2020). https://doi.org/10.1016/j.jmps.2019.103800.

[37]   J.S. Nagra, A. Brahme, J. Lévesque, R. Mishra, R.A. Lebensohn, K. Inal, A new micromechanics based full field numerical framework to simulate the effects of dynamic recrystallization on the formability of HCP metals, Int. J. Plast. 125 (2020) 210–234. https://doi.org/10.1016/j.ijplas.2019.09.011.

[38]   C. Mareau, M.R. Daymond, Micromechanical modelling of twinning in polycrystalline materials: Application to magnesium, Int. J. Plast. 85 (2016) 156–171. https://doi.org/10.1016/j.ijplas.2016.07.007.

[39]   C. Paramatmuni, A.K. Kanjarla, A crystal plasticity FFT based study of deformation twinning, anisotropy and micromechanics in HCP materials: Application to AZ31 alloy, Int. J. Plast. 113 (2019) 269–290. https://doi.org/10.1016/j.ijplas.2018.10.007.

[40]   H.F. Poulsen, Three-Dimensional X-ray Diffraction, Mapping Polycrystals and their Dynamics, Springer, 2004.

[41]   J. Oddershede, S. Schmidt, H.F. Poulsen, H.O. Srensen, J. Wright, W. Reimers, Determining grain resolved stresses in polycrystalline materials using three-dimensional X-ray diffraction, J. Appl. Crystallogr. 43 (2010) 539–549. https://doi.org/10.1107/S0021889810012963.

[42]   H. Abdolvand, J. Wright, A.J. Wilkinson, Strong grain neighbour effects in polycrystals, Nat. Commun. 9 (2018) 171. https://doi.org/10.1038/s41467-017-02213-9.

[43]   H. Abdolvand, J.P. Wright, A.J. Wilkinson, On the state of deformation in a polycrystalline material in three-dimension: Elastic strains, lattice rotations, and deformation mechanisms, Int. J. Plast. 106 (2018) 145–163. https://doi.org/10.1016/j.ijplas.2018.03.006.

[44]   M. Kasemer, P. Dawson, A finite element methodology to incorporate kinematic activation of discrete deformation twins in a crystal plasticity framework, Comput. Methods Appl. Mech. Eng. 358 (2020) 1–29. https://doi.org/10.1016/j.cma.2019.112653.

[45]   C. Liu, P. Shanthraj, J.D. Robson, M. Diehl, S. Dong, J. Dong, W. Ding, D. Raabe, On the interaction of precipitates and tensile twins in magnesium alloys, Acta Mater. 178 (2019) 146–162. https://doi.org/10.1016/j.actamat.2019.07.046.

[46]   Y. Paudel, J. Indeck, K. Hazeli, M.W. Priddy, K. Inal, H. Rhee, C.D. Barrett, W.R. Whittington, K.R. Limmer, H. El, Characterization and modeling of { 10 1, Acta Mater. 183 (2020) 438–451. https://doi.org/10.1016/j.actamat.2019.11.020.

[47]   M. Yaghoobi, J.E. Allison, V. Sundararaghavan, Multiscale modeling of twinning and detwinning behavior of HCP polycrystals, Int. J. Plast. 127 (2020) 102653. https://doi.org/10.1016/j.ijplas.2019.102653.

[48]   H.J. Bong, J. Lee, X. Hu, X. Sun, M.G. Lee, Predicting forming limit diagrams for magnesium alloys using crystal plasticity finite elements, Int. J. Plast. 126 (2020) 102630. https://doi.org/10.1016/j.ijplas.2019.11.009.

[49]   H. Abdolvand, M.R. Daymond, C. Mareau, Incorporation of twinning into a crystal plasticity finite element model: Evolution of lattice strains and texture in Zircaloy-2, Int. J. Plast. 27 (2011) 1721–1738. https://doi.org/10.1016/j.ijplas.2011.04.005.

[50]   R.J. Asaro, a. Needleman, Texture development and strain hardening in rate dependent polycrystals, Acta Metall. 33 (1984) 923–953. https://doi.org/10.1016/0001-6160(85)90188-9.

[51]   C. Tome, G.R. Canova, U.F. Kocks, N. Christodoulou, J.J. Jonas, The relation between macroscopic and microscopic strain hardening in F.C.C. polycrystals, Acta Metall. 32 (1984) 1637–1653. https://doi.org/10.1016/0001-6160(84)90222-0.

[52]   H. Abdolvand, M. Majkut, J. Oddershede, S. Schmidt, U. Lienert, B.J. Diak, P.J. Withers, M.R. Daymond, On the deformation twinning of Mg AZ31B: A three-dimensional synchrotron X-ray diffraction experiment and crystal plasticity finite element model, Int. J. Plast. 70 (2015) 77–97. https://doi.org/10.1016/j.ijplas.2015.03.001.

[53]   F. Xu, R. a. Holt, M.R. Daymond, Modeling lattice strain evolution during uniaxial deformation of textured Zircaloy-2, Acta Mater. 56 (2008) 3672–3687. https://doi.org/10.1016/j.actamat.2008.04.019.

[54]   E.S. Fisher, C.J. Renken, Single-crystal elastic moduli and the hcp ??? bcc transformation in Ti, Zr, and Hf, Phys. Rev. 135 (1964). https://doi.org/10.1103/PhysRev.135.A482.

[55]   H. Abdolvand, M.R. Daymond, Multi-scale modeling and experimental study of twin inception and propagation in hexagonal close-packed materials using a crystal plasticity finite element approach; Part II: Local behavior, J. Mech. Phys. Solids. 61 (2013) 803–818. https://doi.org/10.1016/j.jmps.2012.10.017.

[56]   G. Proust, C.N. Tomé, A. Jain, S.R. Agnew, Modeling the effect of twinning and detwinning during strain-path changes of magnesium alloy AZ31, Int. J. Plast. 25 (2009) 861–880. https://doi.org/10.1016/j.ijplas.2008.05.005.

[57]   M.R. Barnett, N. Stanford, A. Ghaderi, F. Siska, Plastic relaxation of the internal stress induced by twinning, Acta Mater. 61 (2013) 7859–7867. https://doi.org/10.1016/j.actamat.2013.09.024.

[58]   F. Siska, L. Stratil, J. Cizek, A. Ghaderi, M. Barnett, Numerical analysis of twin thickening process in magnesium alloys, Acta Mater. 124 (2017) 9–16. https://doi.org/10.1016/j.actamat.2016.10.068.